GRAPHICAL MODELS AND IMAGE PROCESSING
Vo. 58, No. 5, September, pp. 437–451, 1996
ARTICLE NO. 0036

Reflectance Analysis for 3D Computer Graphics Model Generation

YOICHI SATO[1]

The Robotics Institute, Carnegie Mellon University, Pittsburgh, Pennsylvania 15213

AND

KATSUSHI IKEUCHI

School of Computer Science, Carnegie Mellon University, Pittsburgh, Pennsylvania 15213

Received June 16, 1995; revised May 14, 1996; accepted June 24, 1996

For synthesizing realistic images of a real three dimensional object, reflectance properties of the object surface, as well as the object shape, need to be measured. This paper describes one approach to create a three dimensional object model with physically correct reflectance properties by observing a real object. The approach consists of three steps. First, a sequence of range images and color images is measured by rotating a real object on a rotary table with fixed viewing and illumination directions. Then, the object shape is obtained as a collection of triangular patches by merging multiple range images. Second, by using the recovered object shape, color pixel intensities of the color image sequence are mapped to the object surface and separated into the diffuse and specular reflection components. Finally, the separated reflection components are used to estimate parameters of the Lambertian reflection model and a simplified Torrance–Sparrow reflection model. We have successfully tested our approach using images of a real object. Synthesized images of the object under arbitrary illumination conditions are shown in this paper. © 1996 Academic Press, Inc.

1. INTRODUCTION

Recently, a demand for highly realistic synthesized images has been rapidly increasing in many applications such as virtual reality and virtual museums. To generate realistic images of a three dimensional object, two aspects of information are fundamental: the object's shape and reflectance properties such as color and specularity. These two aspects of information are referred to as the geometric information and the photometric information. Significant improvements have been achieved in the field of computer graphics hardware and image rendering algorithms: however, it is often the case that three dimensional models must be created manually. That input process is normally time-consuming and can be a bottle neck for realistic image synthesis. Therefore, techniques to obtain object models automatically by observing a real object could have a great impact in practical applications.

Techniques for measuring the geometric information by using range data from real objects have received much attention recently. Turk and Levoy developed a system which can merge multiple surface meshes one by one, using two step strategy: registration by the iterative closest-point algorithm (ICP algorithm) and integration by the zippering algorithm [23]. Higuchi *et al.* have developed a method for merging multiple range views of a free-form surface obtained from arbitrary viewing directions, with no initial estimation of relative transformation among those viewing directions [6]. The method is based on the spherical attribute image (SAI) representation of free-form surfaces which was originally introduced by Delingette *et al.* in [4]. Hoppe *et al.* [7] have introduced an algorithm to construct three dimensional surface models from a cloud of points without spatial connectivity. The algorithm differs from others in that it does not require surface meshes as input. It is important to see that those techniques are mainly focused on obtaining the geometric information from range data, but only limited attention has been paid to the photometric information such as reflectance properties.

On the other hand, techniques to obtain the geometric information and the photometric information only from intensity images have been developed by other researchers. Sato and Ikeuchi [18] introduced a method to analyze a sequence of color images taken under a moving light source. They successfully estimated reflectance function parameters as well as object shape by explicitly separating the diffuse and specular reflection components. Subsequently, the technique has been applied to analyze a color image sequence taken in an outdoor environment under solar illumination [19]. Lu and Little developed a method

[1] E-mail: ysato@ri.cmu.edu.

1077-3169/96 $18.00

to estimate a reflectance function from a sequence of black and white images of a rotating smooth object, and the object shape was successfully recovered using the estimated reflectance function [12]. Since the reflectance function is measured directly from the input image sequence, the method does not assume a particular reflection model such as the Lambertian model which is commonly used in computer vision. However, their algorithm can be applied to object surfaces with uniform reflectance properties, and it cannot be easily extended to overcome this limitation. Another interesting attempt for measuring a reflectance function from intensity images has been reported by Ward [24]. Ward designed a special device with a half-silvered hemisphere and a CCD video camera, which can measure a bidirectional reflectance distribution function (BDRF) of anisotoropic reflection. The main advantage of the device is that it takes significantly less time to measure a BDRF than a conventional gonioreflectometer. A BDRF of a real object surface has been measured by the device and highly realistic images are synthesized. However, this approach cannot be easily extended for modeling real objects with various reflectance properties. A small piece of test material has to be given to measure the material's BDRF.

Recently, techniques to measure the geometric and photometric information together by using both range images and black and white intensity images have been studied. Ikeuchi and Sato originally developed a method to measure object shapes and reflection function parameters from a range image and intensity image pair [9]. In their attempt, the surface shape is recovered from the range image at first, and then surface normals of the recovered object surface are used for reflectance parameter estimation. The main drawback of the method is that it assumes uniform reflectance properties over the object surface. Additionally, only partial object shape was recovered because only one range image was used. Kay and Caelli introduced another method to use a range image and four or eight intensity images taken under different illumination conditions [10]. By increasing the number of intensity images, they estimated reflection function parameters locally for each image pixel. Unlike the algorithm proposed by Sato and Ikeuchi, the method can handle object surfaces with varying reflectance properties. However, it is reported that parameter estimation can be unstable especially when the specular reflection component is not observed strongly.

In this paper, we propose one approach to recover both the geometric and photometric information from a sequence of range images and color images of a rotating object. Unlike previously introduced methods, our approach is capable of estimating parameters of a reflection function locally in a robust manner. First, a sequence of range images is used to recover the entire shape of an object as a collection of triangular patches. The zipper system developed by Turk and Levoy [23] is used for the shape recovery stage. Then, a sequence of color images are mapped onto the recovered shape. As a result, we can determine observed color changes through the image sequence for all triangular patches of the object surface. The observed color sequence is separated into the diffuse reflection component and the specular reflection component by the algorithm used originally by Sato and Ikeuchi in [18]. Subsequently, parameters of a reflection function used in our analysis are estimated reliably for the diffuse and specular reflection components. The reflection model used here is described as a linear combination of the Lambertian model and the Torrance–Sparrow model. The Torrance–Sparrow model is modified according to our experimental setup, where the viewing and illumination directions are always the same. Finally, color images of the object are synthesized using the constructed model to demonstrate the feasibility of the proposed approach.

The paper is organized as follows. Section 2.1 describes the recovery of an object shape from a sequence of range images. In Section 2.2, the projection of color images onto the recovered object shape is explained. Section 3.1 introduces the reflection model used in our experiment. The algorithm for separating the diffuse and specular reflection components is explained in Section 3.2, and reflectance parameter estimation is discussed in Section 3.3. The algorithm was applied to range images and color images of a real object, and experimental results are shown in Section 4. Concluding remarks are presented in Section 5.

2. MODELING OF GEOMETRIC INFORMATION

2.1. *Shape Recovery*

In this section, a method for generating a three dimensional object shape from multiple range images is described.

In the past, there have been a large number of techniques investigated for constructing three dimensional object shapes from unorganized or organized points. For instance, Turk and Levoy [23] developed a technique to combine multiple range images one by one, using a two-step strategy: registration and integration. Their technique uses a modified version of the ICP algorithm which was originally developed by Besl and McKay [2]. After the registration procedure, two surface meshes composed of small triangular patches are integrated to produce one combined surface mesh. They called the integration algorithm the *zipper algorithm*. Turk and Levoy's zipper algorithm is effective for producing an object model with a large number of triangular patches. In their paper [23], example objects typically consist of over 100,000 triangle patches. One of the advantages of the zipper system is that it does not require an accurate relative transformation between the range images. That is because the all range images can be aligned by using the ICP algorithm. We found that it is

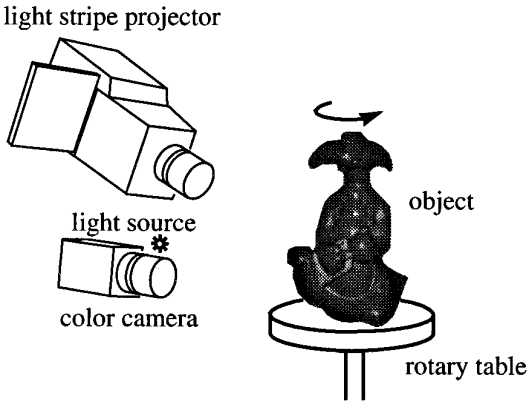

FIG. 1. Experimental setup.

still advantageous even when the relative transformation can be measured directly (e.g., using a rotary table). The zipper system takes surface meshes created from range images at its input. That reduces the complexity of the integration algorithm significantly, while other algorithms use a collection of data points without connectivity information among the points. Because of the zipper system's advantages mentioned here, we used the system for modeling geometric information of real objects. For more details of the zipper system, refer to the paper by Turk and Levoy [23].

Range images are obtained using a light stripe range finder with a liquid crystal shutter and a color CCD video camera [17]. It can compute three dimensional point locations correponding to image pixels based on optical triangulation. For each range image, a set of six images is obtained. Those images contain x, y, and z locations and red, green, and blue color band values of all pixels. Pixels of the range images and the color images correspond because all images are captured by using the same camera. The experimental setup used in our experiments is illustrated in Fig. 1. A single-point light source is used for illuminating a target object. The light source is located near the camera lens so that both the viewing direction and the illumination direction are approximately the same. This light source location is chosen to avoid the problem of self-shadowing in our images. A similar light source setting was also used by Lu and Little [12].

First, the range finder is calibrated by using a calibration box of known size and shape. The calibration produces a 4×3 matrix which represents the projection transformation between the world coordinate system and the image coordinate system. The projection transformation matrix will be used for mapping a sequence of input color images onto the recovered object shape (Section 2.2). The object whose shape and reflectance information are to be recovered is placed on a computer-controlled rotary table. Then, range and color images are captured by the range finder at fixed angle steps of object orientation. Each range image is used for creating a surface mesh which consists of small triangular patches. Following the measurement of range and color images, the zipper system is used for combining all surface meshes to create a merged object shape. The recovered object shape and a sequence of input color images will be used for analyzing the object's reflectance properties later. Reflectance property analysis will be explained in Section 3.

2.2. *Mapping Color Images onto Recovered Object Shape*

The recovered object shape and the sequence of input color images are used for estimating reflection model parameters at each triangular patch. The algorithm to estimate reflectance parameters of the object surface from the sequence of color images will be explained in Section 3.

For the reflectance parameter estimation, we need to know how the observed color changes at each triangular patch as the object rotates. This can be done by mapping the sequence of color images onto the recovered object shape. The recovered object shape, a collection of triangular patches, is defined in a three dimensional world coordinate system. The rotary table's location and orientation in the world coordinate system are known from a previous calibration stage. Thus, locations of all triangular patches in the world coordinate system can be easily computed for each orientation of the object. Subsequently, the triangular patches are projected back onto the image plane using the 4×3 perspective camera projection matrix. The center of the projection is simply computed from the projection matrix [21]. The Z-buffer algorithm is used for determining visible triangular patches and their locations on the image plane. Ideally, all triangular patches are small enough to have uniform color on the image plane. However, a projection of a triangular patch on the image plane often corresponds to multiple image pixels of different color. Therefore, we average the color intensity of all corresponding pixels, and the average intensity is assigned to the triangular patch. It would be a straightforward extension to assign a two dimensional array to each triangular patch to store all pixel colors when the resolution of triangular patches is high enough.

By applying the procedure explained above for all object orientations, we finally get a collection of triangular patches each of which has a sequence of observed colors with respect to the object orientation.

3. MODELING OF PHOTOMETRIC INFORMATION

3.1. *Reflection Model*

In this section, we describe the reflectance model used in this work. The reflectance model will be used later for

separating the diffuse and surface components from a sequence of color images. The reflection component separation is described in Section 3.2. The model will also be used for reflectance parameter estimation which is explained in Section 3.3.

A mechanism of reflection is described in terms of three reflection components, namely the diffuse lobe, the specular lobe, and the specular spike [13]. The diffuse lobe component is explained as internal scattering. When an incident light ray penetrates the object surface, it is reflected and refracted repeatedly at a boundary between small particles and medium of the object. The scattered light ray eventually reaches the object surface, and is refracted into the air in various directions. This phenomenon results in the diffuse lobe component. The Lambertian model is based on the assumption that those directions are evenly distributed in all directions. In this paper, the Lambertian model is used for modeling the diffuse lobe component.

Unlike the diffuse lobe and the specular lobe components, the specular spike component is not commonly observed in many actual applications. The component can be observed only from mirror-like smooth surfaces where reflected light rays of the specular spike component are concentrated in a specular direction. This makes it hard to observe the specular spike component from viewing directions at coarse sampling angles. Therefore, in many computer vision and computer graphics applications, a reflection mechanism is modeled as a linear combination of two reflection components: the diffuse lobe component and the specular lobe component. Those two reflection components are normally called the diffuse reflection component and the specular reflection component, respectively. The reflection model was formally introduced by Shafer as the dichromatic reflection model [20]. Based on the dichromatic reflection model, the reflection model used in our analysis is represented as a linear combination of the diffuse reflection component and the specular reflection component. The Lambertian model and the Torrance–Sparrow model are used for modeling those two reflection components, respectively. As Fig. 1 illustrates, illumination and viewing directions are fixed and the same. The reflection model used for the particular experiment setup is given as

$$I_m = K_{D,m} \cos\theta + K_{S,m} \frac{1}{\cos\theta} e^{-\theta^2/(2\sigma_\alpha^2)} \quad m = R, G, B, \quad (1)$$

where θ is the angle between the surface normal and the viewing direction (or the light source direction) (Fig. 17), $K_{D,m}$ and $K_{S,m}$ are a constant for each reflection component, σ_α is the standard deviation of a facet slope α of the Torrance–Sparrow model. The derivation is shown in the appendices of this paper. The direction of the light source and the camera with respect to the surface normal is referred to as the sensor direction θ in this paper. In our analysis, reflection bounced only once from the light source is considered. Therefore, the reflection model is valid only for convex objects, and it cannot represent reflection which bounces more than once (i.e., interreflection) on concave object surfaces. We empirically found that interreflection did not affect our analysis significantly.

3.2. *Reflection Component Separation*

The algorithm to separate the two reflection components is described here. The separation of the diffuse and specular reflection components is important for robust estimation of reflectance parameters. It has been reported that estimating all reflectance parameters at once tends to make computation unstable [10]. Therefore, the separation algorithm is applied prior to reflectance parameter estimation. The separation algorithm was originally introduced for the case of a moving light source by Sato and Ikeuchi in [18]. In this paper, a similar algorithm is applied for the case of a moving object.

Using three color bands; red, green, and blue, the coefficients $K_{D,m}$ and $K_{S,m}$, in Eq. (1), become two linearly independent vectors, $\mathbf{K}_D$ and $\mathbf{K}_S$, unless the colors of the two reflection components are accidentally the same:

$$\mathbf{K}_D = \begin{bmatrix} K_{D,R} \\ K_{D,G} \\ K_{D,B} \end{bmatrix} = \begin{bmatrix} g \int_\lambda \tau_R(\lambda) k_D(\lambda) s(\lambda)\, d\lambda \\ g \int_\lambda \tau_G(\lambda) k_D(\lambda) s(\lambda)\, d\lambda \\ g \int_\lambda \tau_B(\lambda) k_D(\lambda) s(\lambda)\, d\lambda \end{bmatrix} \quad (2)$$

$$\mathbf{K}_S = \begin{bmatrix} K_{S,R} \\ K_{S,G} \\ K_{S,B} \end{bmatrix} = \begin{bmatrix} g \int_\lambda \tau_R(\lambda) k_S(\lambda) s(\lambda)\, d\lambda \\ g \int_\lambda \tau_G(\lambda) k_S(\lambda) s(\lambda)\, d\lambda \\ g \int_\lambda \tau_B(\lambda) k_S(\lambda) s(\lambda)\, d\lambda \end{bmatrix}. \quad (3)$$

These two vectors represent the colors of the diffuse and specular reflection components in the dichromatic reflectance model [20].

First, the color intensities in the R, G, and B channels from n input images of the object are mapped to each triangular patch of the object model (See Section 2.2.) It is important to note that all intensities are measured *at the same triangular patch*. The three sequences of intensity values are stored in the columns of an $n \times 3$ matrix M. Considering the reflectance model and two color vectors in Eqs. (1)–(3), the intensity values in the R, G, and B channels can be represented as

$$
\begin{aligned}
M &= [\mathbf{M}_R \mathbf{M}_G \mathbf{M}_B] \\
&= \begin{bmatrix} \cos\theta_1\, P(\theta_1) \\ \cos\theta_2\, P(\theta_2) \\ \cdot \quad \cdot \\ \cdot \quad \cdot \\ \cos\theta_n\, P(\theta_n) \end{bmatrix} \begin{bmatrix} K_{D,R} K_{D,G} K_{D,B} \\ K_{S,R} K_{S,G} K_{S,B} \end{bmatrix} \\
&= [\mathbf{G}_D \mathbf{G}_S] \begin{bmatrix} \mathbf{K}_D^T \\ \mathbf{K}_S^T \end{bmatrix} \\
&= GK,
\end{aligned} \tag{4}
$$

where $P(\theta) = (\exp(-\theta^2/\sigma_\alpha^2))/\cos\theta$, and the two vectors $\mathbf{G}_D$ and $\mathbf{G}_S$ represent the intensity values of the diffuse and specular reflection components with respect to the sensor direction θ. The vector $\mathbf{K}_D$ represents the diffuse reflection color vector. The vector $\mathbf{K}_S$ represents the specular reflection color vector. We call the two matrices G and K, the *geometry matrix* and the *color matrix*, respectively.

Suppose we have an estimate of the color matrix K. Then, the two reflection components represented by the geometry matrix G are obtained by projecting the observed reflection stored in M onto the two color vectors $\mathbf{K}_D$ and $\mathbf{K}_S$.

$$G = MK^+, \tag{5}$$

where K^+ is a 3×2 pseudoinverse matrix of the color matrix K.

The derivation shown above is based on the assumption that the color matrix K is known. In our experiments, the specular reflection color vector $\mathbf{K}_S$ is directly measured by calibration. Therefore, only the diffuse color vector $\mathbf{K}_D$ is unknown. The method to estimate the diffuse color vector is explained in the following section.

3.2.1. *Estimation of the Diffuse Reflection Color.* From Eq. (1), it can be seen that the distribution of the specular reflection component is limited to a fixed angle, depending on σ_α. Therefore, if two vectors, $\mathbf{w}_i = [I_{Ri} I_{Gi} I_{Bi}]^T$ $(i = 1, 2)$ are sampled on the θ axis at large enough interval, at least one of these vectors will be equal to the color vector of the diffuse reflection component $\mathbf{K}_D^T$ (i.e., it has no specular reflection component). The desired color vector of the diffuse reflection component $\mathbf{K}_D^T$ is the vector $\mathbf{w}_i$ which subtends the largest angle with respect to the vector $\mathbf{K}_S^T$. The angle between the two color vectors can be calculated as

$$\beta = \operatorname{acos} \frac{\mathbf{K}_S^T \cdot \mathbf{w}_i}{|\mathbf{K}_S^T||\mathbf{w}_i|}. \tag{6}$$

Once we get the color matrix K, the geometry matrix G can be calculated from Eq. (5). Each of the diffuse and specular reflection components is then given as

$$M_D = \mathbf{G}_D \mathbf{K}_D^T \tag{7}$$

$$M_S = \mathbf{G}_S \mathbf{K}_S^T. \tag{8}$$

3.3. *Reflectance Parameter Estimation for Segmented Regions*

In the previous section, the method to separate the two reflection components from a sequence of observed colors of each triangular patch was described. In this section, we will discuss how to estimate parameters of the reflectance model for the triangular patch by using the separated reflection components.

By applying the separation algorithm as explained above, we obtain a sequence of the diffuse reflection intensities and a sequence of the specular reflection intensities for each triangular patch. This information is sufficient to estimate reflectance parameters of the reflection model Eq. (1) separately for the two reflection components. As Eq. (1) shows, the reflectance model is a function of the angle between the surface normal and the viewing direction θ. Therefore, for estimating reflectance parameters: $K_{D,m}$, $K_{S,m}$, and σ_α, the angle θ has to be computed as the rotary table rotates. Since the projection transformation matrix is already given and the object orientation is known in the world coordinate system, it is straightforward to compute a surface normal vector and a viewing direction vector (or an illumination vector) at a center of each triangular patch. Thus, the angle θ between the surface normal and the viewing direction vector can be computed. After the angle θ is computed, the reflectance parameters for the diffuse reflection component ($K_{D,m}$) and the specular reflection component ($K_{S,m}$ and σ_α) are estimated separately by the Levenberg–Marquardt method [16]. In our experiment, the camera output is calibrated so that the specular reflection color has the same value from the three color channels. Therefore, only one color band is used to estimate K_S in our experiment.

By repeating the estimation procedure for all triangular patches, we can estimate the diffuse reflection component parameters for all triangular patches if those patches are illuminated in one or more frames of the image sequence. On the other hand, the specular reflection component can be observed only in a limited viewing direction. Due to this fact, the specular reflection component can be observed only in a small subset of all triangular patches. We cannot estimate the specular reflection component parameters for those patches in which the specular reflection component is not observed. Even if the specular reflection component is observed, the parameter estimation can become unreliable if the specular reflection is not sufficiently

strong. To avoid that, we can increase the number of sampled object orientations and take more color images. However, that still cannot guarantee that all triangular patches show the specular reflection component. Taking more color images may not be practical since more sampled images require more measurement time and data processing time.

For the above reasons, we decided to assign the specular reflection component parameters based on region segmentation. In our experiments, it is assumed that the object surface can be segmented into a finite number of regions which have uniform diffuse color, and all triangular patches within each region have the same specular reflection component parameters. By using the segmentation algorithm, the specular reflection parameters of each region can be estimated from triangular patches with strong specularity. The estimated parameters are assigned to the rest of patches in the region. The triangular patches with strong specularity can be easily selected after the reflectance component separation explained in Section 3.2. The limitation of this approach is that the specular reflection parameters for a region cannot be estimated if no specularity is observed in the region. In that case, the specular reflection parameters of neighboring regions can be assigned to the region as an approximation. It is important to note that the segmentation and parameter estimation are used only for the specular reflection component. The diffuse reflection component parameters are estimated locally regardless of specularity.

After reflectance parameters are estimated for all triangular patches, we have the object shape as a collection of triangular patches and reflectance parameters for those patches. This information can be used for synthesizing computer graphics images with physically correct reflection. Some examples of synthesized images will be shown in Section 4.7.

4. EXPERIMENTAL RESULTS

4.1. *Experimental Setup*

In the previous sections, we described the method to obtain shape and reflectance information from multiple range images and color images. The method includes three steps: (1) merging multiple triangular surface patches into one patch to generate an object shape model, (2) separating the two fundamental reflection components from a sequence of color images, and (3) estimating the reflection model parameters from the separated reflection components. We applied the method to real range and color images taken in a laboratory setup in order to demonstrate the feasibility of the proposed method. A SONY CCD color video camera module model XC-711 is used to take color images in our experiments. A light stripe projector with a liquid crystal shutter is used for taking range images. The same color camera is used to take color images and range images. This guarantees correspondence between the range images and the color images at each pixel. The target object used in our experiment is a plastic dinosaur with an approximate height of 170 mm. The object is painted in several colors, and each painted surface region appears to have a uniform color. The object is located on a rotary table whose orientation can be controlled by a computer. Multiple range and color images of the object are taken for different object orientations. A single xenon lamp whose diameter is approximately 10 mm is used as a point light source. The light source is located near the camera, and the light source direction is considered to be the same as the viewing direction. The camera and light source locations are fixed in our experiment. The approximate distance between the object and the camera is 2 m. Our experimental setup is ilustrated in Fig. 1.

The range finder is calibrated to obtain the 4×3 projection matrix between the world coordinate system and the image coordinate system. The matrix is used for mapping the color images onto the recovered object shape. The location and orientation of the rotary table in the world coordinate system is also measured using a calibration box and the range finder. As a result, the direction and location of the rotation axis in the world coordinate system are known. They are used for projecting the color images onto the recovered object shape as described in Section 2.2. The color video camera is calibrated to ensure linear response from all three color bands. A color chart is also used for measuring the light source color. Therefore, the illumination color is assumed to be known in our experiment.

4.2. *Measurement*

Range images and color images of the target object are taken using the experimental setup described in the previous section. The object is placed on the rotary table, and range images and color images are captured as the object rotates on the table. In our experiment, range images are captured at 45° intervals (8 images total), and color images are obtained as 3° intervals (120 images total). The reason why we need more color images than range images is because fine sampling is necessary to capture the specular reflection distribution correctly. On the other hand, the range images are used only for recovering the object shape, and it does not require fine sampling. The small number of images are sufficient to observe the object shape entirely. Two frames of the input range images are shown as triangular surface patches in Fig. 2. Figure 3 shows the sequence of input color images. Six frames out of 120 are shown as examples.

4.3. *Shape Recovery*

The zipper system [23] was used for merging eight triangular surface meshes created from the input range images.

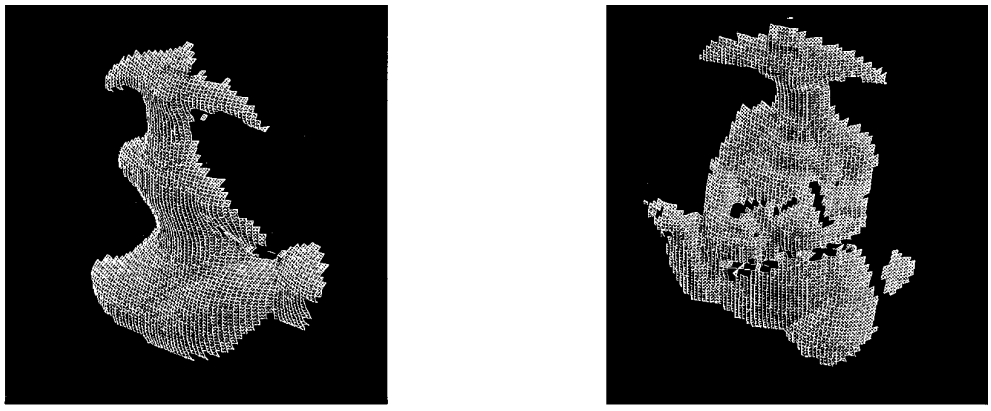

FIG. 2. Input range data (2 out of 8 frames).

The recovered object shape is shown in Fig. 4. The object shape consists of 9943 triangular patches. In the process of merging surface meshes, the object shape was manually edited to remove noticeable defects such as holes and spikes. Manual editing can be eliminated if more range images are used.

4.4. *View Mapping*

After the object shape is generated from the range images, the sequence of color images is mapped onto the recovered object shape as described in Section 2.2. The result of the color image mapping is illustrated in Fig. 5. Six frames are shown as examples here.

Based on the image mapping onto the recovered object shape, a sequence of observed colors is determined at each triangular patch of the object shape as explained in Section 2.2. The observed color is not defined if the triangular patch is not visible from the camera. In this case, the observed color is set to zero. Figure 6 illustrates a typical observed color sequence at a triangular patch with strong specularity. The specular reflection component can be observed strongly near image frame 67. When the specular reflection component exists, the output color intensity is a linear combination of the diffuse reflection component and the specular reflection component. The two reflection components are separated by using the algorithm explained in Section 3.2, and the separation result will be shown in the next section. The intensities are set to zero before image frame 39 and after image frame 92 because the triangular patch is not visible from the camera due to occlusion. Another example with weak specularity is shown in Fig. 7. In the example, the observed specular reflection is relatively small compared to the diffuse reflection component. As a result, estimating reflectance parameters for both the diffuse and specular reflection components together could be sensitive to various disturbances such as image noise. That is why the reflection component separation is introduced in prior to parameter estimation in our analysis. By separating the two reflection components based on color, reflectance parameters can be estimated separately in a robust manner.

4.5. *Reflection Component Separation*

The algorithm to separate the diffuse and specular reflection components, described in Section 3.2, was applied to the observed color sequence at each triangular patch. The red, green, and blue intensities of the observed color sequence are stored in the matrix M as it columns Eq. (4). Then, the matrix G is computed from the matrix M and the matrix K which is estimated as described in Section 3.2.1. Finally, the diffuse and specular reflection components are given as shown in Eqs. (7) and (8). This reflection component separation is repeated for all triangular patches of the object. Some of the separation results are shown in Figs. 8 and 9. Figure 8 shows the separated reflection components with strong specularity. The measured color sequence is shown in Fig. 6 in the previous section. Another example of the reflection component separation is given in Fig. 9. In that case, the specular reflection component is relatively small compared to the diffuse reflection component. That example indicates that the separation algorithm can be applied robustly even if the specularity is not observed strongly. After the reflection component separation, reflectance parameters can be estimated separately. The result of parameter estimation will be shown in Section 4.6.

The separated reflection components at all triangular patches of a particular image frame can be used to generate the diffuse reflection image and the specular reflection image. The result of the diffuse and specular reflection

frame 0

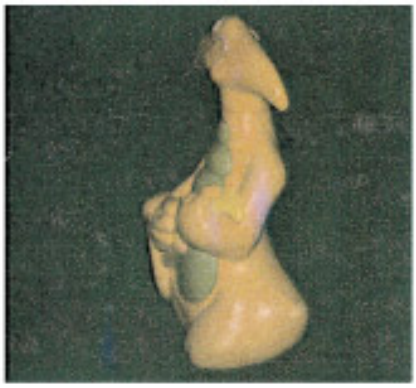

frame 20

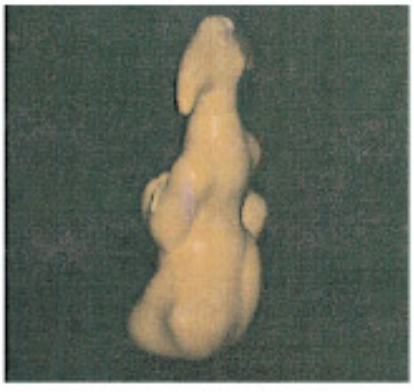

frame 40

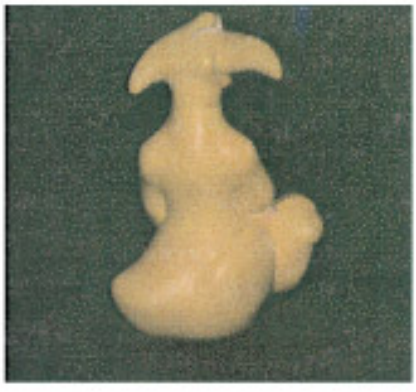

frame 60

frame 80

frame 100

FIG. 3. Input color images.

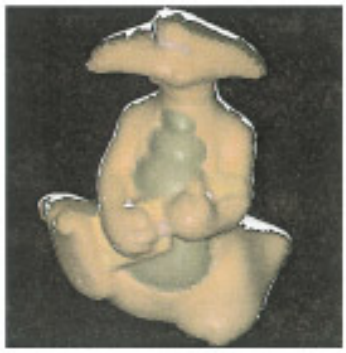

frame 0

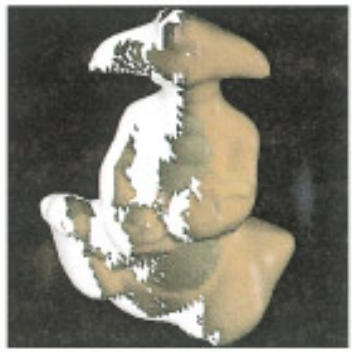

frame 20

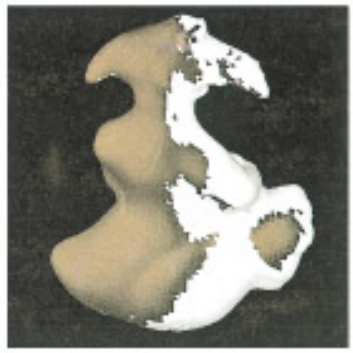

frame 40

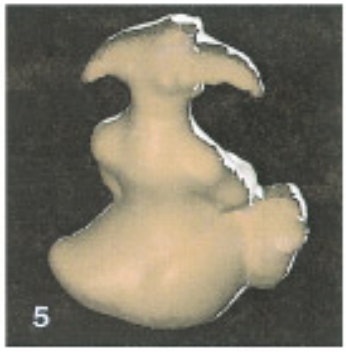

frame 60

frame 80

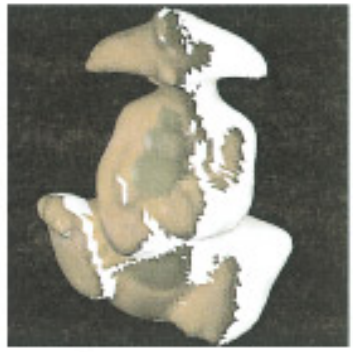

frame 100

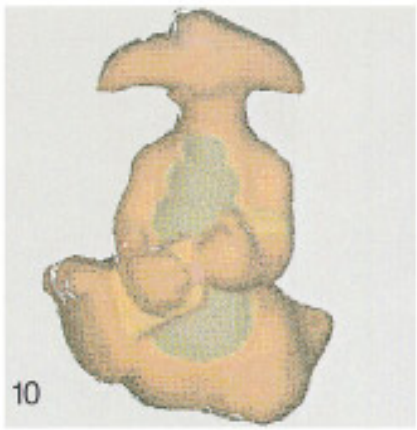

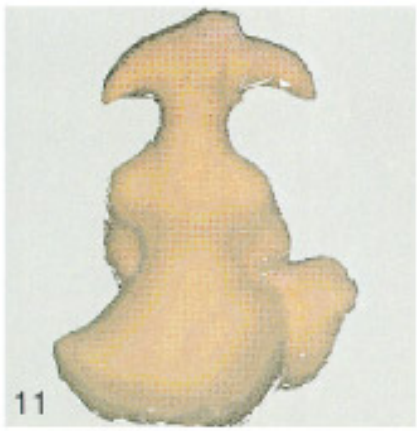

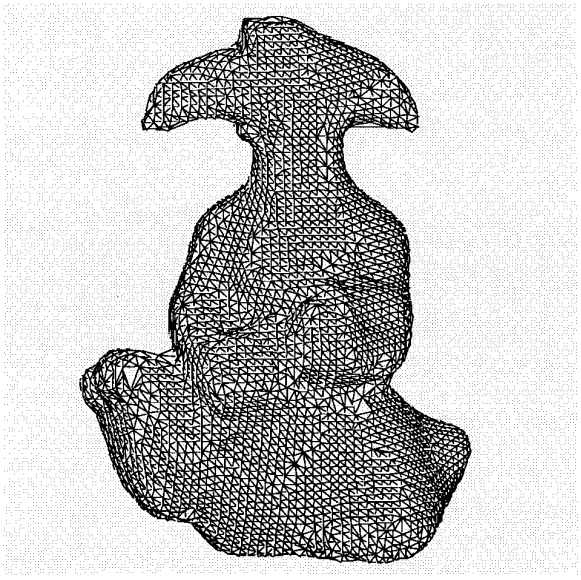

FIG. 4. Recovered object shape.

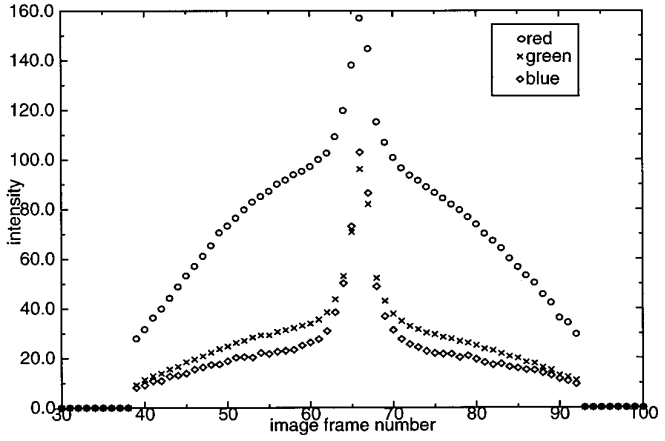

FIG. 6. Intensity change with strong specularity.

images are shown in Figs. 10 and 11. Image frames 0 and 60 are used to generate Figs. 10 and 11, respectively.

4.6. *Reflectance Parameter Estimation for Segmented Regions*

By using the separated diffuse reflection components of all triangular patches, the object surface was segmented based on the hue of the diffuse reflection components, as explained in Section 3.3. The result of the region segmentation is shown in Fig. 12 (segmented regions are represented as gray levels). For estimating specular reflection component parameters, 10 triangular patches with the largest specular reflection component are selected for each of the segmented regions. Then, the specular reflection component parameters of the reflection model Eq. (1) are estimated by the Levenberg–Marquardt method for each of the 10 selected triangular patches. Finally, the average of the estimated parameters of the selected triangular patches is used as the specular reflection component parameters of the segmented region. The estimated specular reflection parameters are assigned to all triangular patches within the segmented region. In our experiments, the 4 largest segmented regions were used for specular reflection parameter estimation, and the rest of the small regions were not used. The small regions were found to be located near or at the boundaries of the large regions. Hence, a surface normal of a triangular patch does not necessarily represent a surface normal of the object surface at the location. That causes the estimation to be inaccurate. Therefore, those small regions are assumed to have the same specular reflection properties as the large regions in our analysis. The result of the estimated specular reflection component parameters is shown in Table 1.

Unlike the specular reflection parameter estimation, parameters of the diffuse reflection component are estimated for each triangular patch individually. That is because the diffuse reflection component at the triangular patch is guaranteed to be observed as long as the patch is illuminated and not occluded from the viewing direction. The result of the diffuse reflection component parameter estimation will be shown in the next section as synthesized images of the object.

4.7. *Synthesized Images with Correct Reflection*

By using the recovered object shape and reflection model parameters, images of the object under arbitrary illumination conditions can be generated. In this section, some of the images are shown to demonstrate the ability of the proposed method to produce highly realistic images. Point light sources located far from the object are used for generating images. For comparing synthesized images with the real images of the object, the object model was rendered with illumination and viewing directions similar to those in our experimental setup. The illumination and viewing

FIG. 5. View mapping result.

FIG. 10. Diffuse image and specular image: example 1.

FIG. 11. Diffuse image and specular image: example 2.

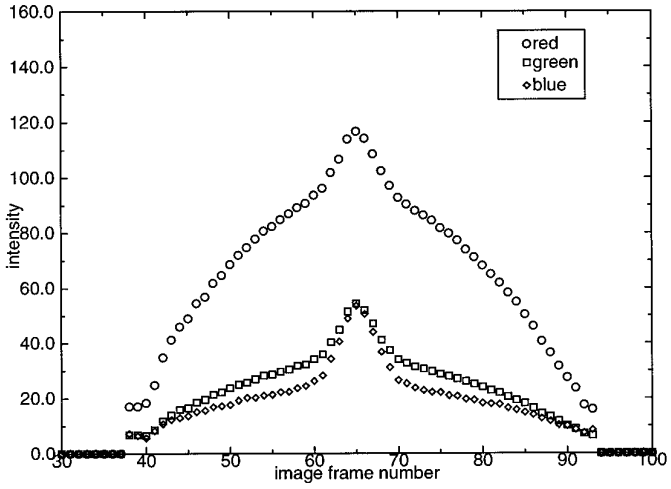

FIG. 7. Intensity change with little specularity.

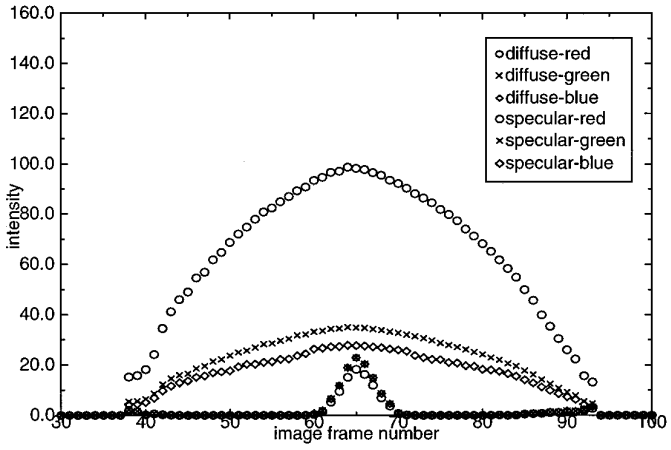

FIG. 9. Separated reflection component with little specularity.

directions for input color image frame 0 were used to create Fig. 13. The input color image is shown in Fig. 3. It is important to see that region 2 shows less specularity than region 0 and region 1. (See Fig. 12 for region numbers.) In addition, the specular reflection is widely distributed in region 2 because region 2 has a large reflectance parameter σ_α. Another example image is shown in Fig. 14. The object model is rendered under illumination and viewing conditions similar to input color image frame 60. Figure 15 shows the object illuminated by two light sources. The arrow in the image represents the illumination direction.

5. CONCLUSION

We have studied an approach for creating a three dimensional object model with physically correct reflectance properties by observing a real object. The Lambertian model and the Torrance–Sparrow reflection model are used as the basic reflectance models in our analysis. The object is located on a rotary table, and a sequence of range and color images are taken as the object rotates. First, the object shape is recovered from a range image sequence as a collection of triangular patches. Then a sequence of input color images are mapped onto the recovered object shape to determine an observed color sequence at each triangular patch individually. The observed color sequence is separated into the diffuse and specular reflection components. Finally, parameters of the Lambertian model and the Torrance–Sparrow model are estimated separately at each of the triangular patches. By using the recovered object shape and estimated reflectance parameters associated with each triangular patch, highly realistic images of the real object

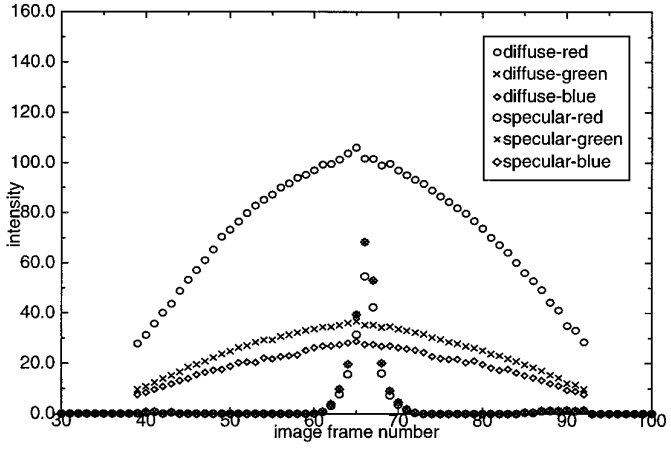

FIG. 8. Separated reflection components with strong specularity.

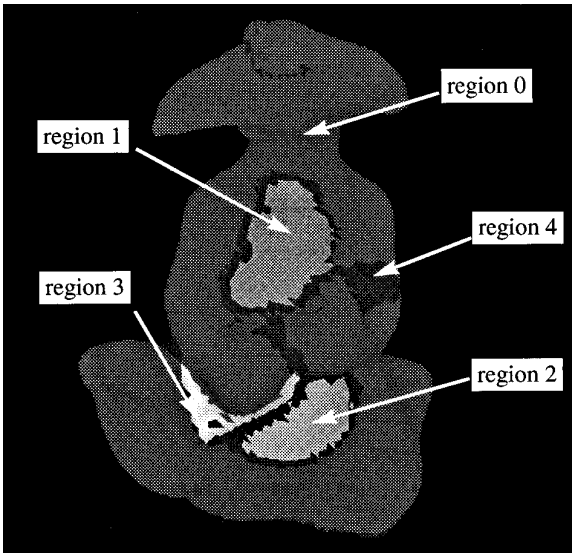

FIG. 12. Segmentation result (gray levels represent regions).

TABLE 1
Estimated Parameters of the Specular Reflection Component

Region no.	K_S	σ_α
0	134.58	0.091
1	111.32	0.119
2	38.86	0.147
3	39.87	0.177

can be synthesized under arbitrary illumination conditions. The proposed approach has been applied to real range and color images of a plastic object, and the effectiveness of the proposed approach has been successfully demonstrated by constructing synthesized images of the object under different illumination conditions.

APPENDIX A

Simplified Torrance–Sparrow Model

In our work, the Torrance–Sparrow model [22] is used for representing the specular lobe reflection component.

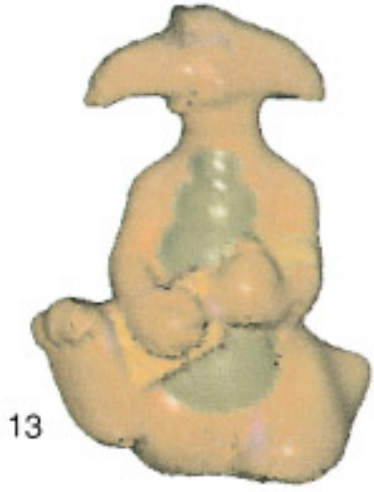

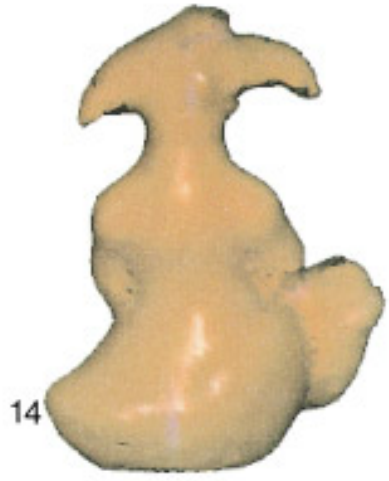

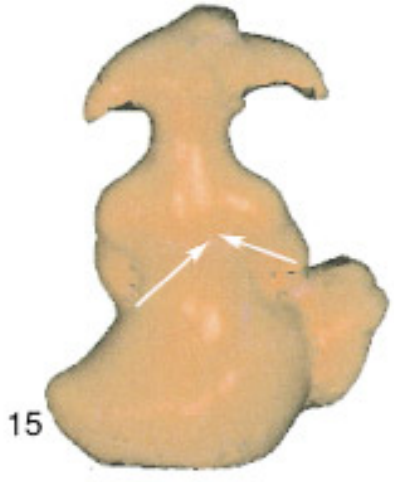

FIG. 13. Synthesized image 1.

FIG. 14. Synthesized image 2.

FIG. 15. Synthesized image 3.

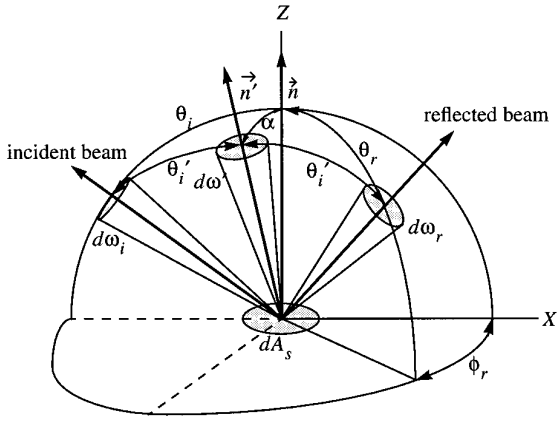

FIG. 16. Geometry for the Torrance–Sparrow model.

The model describes single reflection of incident light rays by rough surfaces. This model is reported to be valid when the wavelength of light is much smaller than the roughness of the surface [22], which is always true in our experiments. The surface is modeled as a collection of planar micro-facets which are perfectly smooth and reflect light rays as perfect specular reflectors. The geometry for the Torrance–Sparrow model is shown in Fig. 16. The surface area dA_s is located at the center of the coordinate system. An incoming light beam lies in the X–Z plane and is incident to the surface at an angle θ_i. The radiance and solid angle of the light source are represented as L_i and $d\omega_i$, respectively. In the Torrance–Sparrow model, the micro-facet slopes are assumed to be normally distributed. Additionally, the distribution is assumed to be symmetric around the mean surface normal $\vec{n}$. The distribution is represented by a one-dimensional normal distribution

$$\rho_\alpha(\alpha) = ce^{-\alpha^2/(2\sigma_\alpha^2)}, \tag{9}$$

where c is a constant, and the facet slope α has mean value $\langle\alpha\rangle = 0$ and standard deviation σ_α. In the geometry shown in Fig. 16, only planar micro-facets having normal vectors within the solid angle $d\omega'$ can reflect incoming light flux specularly. The number of facets per unit area of the surface that are oriented within the solid angle $d\omega'$ is equal to $\rho_\alpha(\alpha)\, d\omega'$. Hence, considering the area of each facet a_f and the area of the illuminated surface dA_s, the incoming flux on the set of reflecting facets is determined as

$$d^2\Phi_i = L_i\, d\omega_i (a_f \rho_\alpha(\alpha)\, d\omega'\, dA_s) \cos\theta_i'. \tag{10}$$

The Torrance–Sparrow model considers two terms to determine what portion of the incoming flux is reflected as outgoing flux. One term is the Fresnel reflection coefficient, $F(\theta_i', \eta', \lambda)$ where η' is the refractive index of the material, and λ is the wavelength of the incoming light. Its value for a perfect mirror-like surface depends on wavelength, incident angle, and material. The other term is called the geometric attenuation factor, and it is represented as $G(\theta_i, \theta_r, \phi_r)$. It accounts for the fact that at large incidence angles light incoming to a facet may be shadowed by adjacent surface irregularities, and outgoing light along the viewing direction that grazes the surface may be masked or interrupted in its passage to the viewer. Considering those two factors, the flux $d^2\Phi_r$ reflected into the solid angle $d\omega_r$ is determined as

$$d^2\Phi_i = F(\theta_i', \eta', \lambda) G(\theta_i, \theta_r, \phi_r)\, d^2\Phi_i. \tag{11}$$

The radiance of reflected light is defined as

$$dL_{S,r} = \frac{d^2\,\phi_r}{d\omega_r\, dA_s \cos\theta_r}. \tag{12}$$

Substituting Eqs. (10) and (11) into Eq. (12), we obtain

$$dL_{S,r} = \frac{F(\theta_i', \eta', \lambda) G(\theta_i, \theta_r, \phi_r) L_i\, d\omega_i (a_f \rho_\alpha(\alpha)\, d\omega'\, dA_s) \cos\theta_i'}{d\omega_r\, dA_s \cos\theta_r}. \tag{13}$$

Since only facets with normals that lie within the solid angle $d\omega'$ can reflect light into the solid angle $d\omega_r$, the two solid angles are related as

$$d\omega' = \frac{d\omega_r}{4\cos\theta_i'}. \tag{14}$$

Substituting Eq. (14) into Eq. (13), the surface radiance of the surface dA_s given by the specular reflection component is represented as

$$dL_{S,r} = \frac{c a_f F(\theta_i', \eta', \lambda) G(\theta_i, \theta_r, \phi_r)}{4} \frac{L_i\, d\omega_i}{\cos\theta_r} e^{-\alpha^2/(2\sigma_\alpha^2)}. \tag{15}$$

As stated above, the Fresnel coefficient $F(\theta_i', \eta', \lambda)$ and the geometrical attenuation factor $G(\theta_i, \theta_r, \phi_r)$ depend on the illumination and viewing geometry. In our experiments, the geometry is simplified because the viewing direction and the illumination direction always coincide. The simplified geometry is shown in Fig. 17. Substituting $\theta_i = \theta_r = \alpha$, $\theta_i' = 0$, and $\phi_r = \pi$, Eq. (15) is simplified to

$$dL_{S,r} = \frac{c a_f F(0, \eta', \lambda) G(\theta_i, \theta_i, \pi)}{4} \frac{L_i\, d\omega_i}{\cos\theta_i} e^{-\theta_i^2/(2\sigma_\alpha^2)}. \tag{16}$$

It is observed that the geometrical attenuation factor G equals unity for angles of incidence not near the grazing angle. Since that is not the case in our experiment, the geometrical attenuation factor G is assumed to be constant in our analysis. The Fresnel coefficient can be regarded as a function of the wavelength λ because the local angle of incidence θ_i' is always equal to 0. Finally, the surface radiance of the specular reflection component in our experiments is represented as

$$dL_{S,r} = \frac{ca_f F(\lambda) G}{4} \frac{L_i \, d\omega_i}{\cos \theta_i} e^{-\theta_i^2/(2\sigma_\alpha^2)}. \tag{17}$$

The dichromatic reflection model [20] predicts that a reflection mechanism is modeled as a linear combination of two reflection components: the diffuse reflection component and the specular reflection component. According to the dichromatic reflection model, the reflection model used in this paper is represented as a combination of the Lambertian model and Eq. (17)

$$dL_r = \left\{ k_D(\lambda) \cos \theta_i + \frac{k_S(\lambda)}{\cos \theta_i} e^{-\theta_i^2/(2\sigma_\alpha^2)} \right\} L_i \, d\omega_i, \tag{18}$$

where $k_D(\lambda)$ represents the ratio of the radiance to the irradiance of the diffuse reflection, and $k_{\text{spec}}(\lambda) = ca_f F(\lambda) G/4$. That expression is integrated in the case of a collimated light source to produce

$$L_r = \int_{\omega_i} dL_r = k_D(\lambda) s(\lambda) \cos \theta + \frac{k_S(\lambda) s(\lambda)}{\cos \theta} e^{-\theta_i^2/(2\sigma_\alpha^2)}, \tag{19}$$

where $s(\lambda)$ is the surface irradiance on a plane perpendicular to the light source direction.

APPENDIX B

Image Formation Model

If the object distance is much larger than the focal length and the diameter of the entrance pupil of the imaging system, it can be shown that the image irradiance E_p is proportional to scene radiance L_r. It is given as

$$E_p = L_r \frac{\pi}{4} \left(\frac{d}{f} \right)^2 \cos^4 \gamma, \tag{20}$$

where d is the diameter of a lens, f is the focal length of the lens, and γ is the angle between the optical axis and the line of sight [8]. In our experiments, changes of these three parameters d, f, and γ are assumed to be relatively small. Therefore, Eq. (20) can be simply given as

$$E_p = g L_r, \tag{21}$$

where

$$g = \frac{\pi}{4} \left(\frac{d}{f} \right)^2 \cos^4 \gamma.$$

Combining Eqs. (19) and (21), we have

$$E_p = g k_D(\lambda) s(\lambda) \cos \theta + \frac{g k_S(\lambda) s(\lambda)}{\cos \theta} e^{\theta^{-2}/(2\sigma_\alpha^2)}. \tag{22}$$

Now let $\tau_m(R, G, B)$ be the spectral responsivity of the color camera in red, green, and blue bands. Then, the output from the color camera in each band can be expressed as

$$I_m = \int_\lambda \tau_m(\lambda) E_p(\lambda) \, d\lambda. \tag{23}$$

This equation can be simplified as

$$I_m = K_{D,m} \cos \theta + K_{S,m} \frac{1}{\cos \theta} e^{-\theta^2/(2\sigma_\alpha^2)}, \tag{24}$$

where

$$\begin{aligned} K_{D,m} &= g \int_\lambda \tau_m(\lambda) k_D(\lambda) s(\lambda) \, d\lambda \\ K_{S,m} &= g \int_\lambda \tau_m(\lambda) k_S(\lambda) s(\lambda) \, d\lambda. \end{aligned} \tag{25}$$

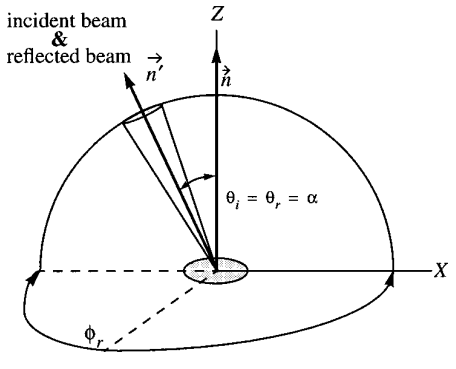

FIG. 17. Geometry for simplified Torrance–Sparrow model.

APPENDIX C

Nomenclature

I_m	camera intensity in m band
$K_{D,m}$, $K_{S,m}$	constants for each reflection component in m band
θ, α, θ_i, θ_i', θ_r, ϕ_r, γ	various angles

σ_α	standard deviation of a facet slope α
m	color band = red, green, blue
$\mathbf{K}_D$, $\mathbf{K}_S$, $\mathbf{G}_D$, $\mathbf{G}_S$	rows and columns of matrices K and G
g	constant from Eq. (21)
λ	light wave frequency
$\tau_R(\lambda)$, $\tau_G(\lambda)$, $\tau_B(\lambda)$	camera spectral responsivity
$k_D(\lambda)$, $k_S(\lambda)$	ratio of radiance to irradiance for the diffuse and specular components
$s(\lambda)$	surface irradiance
M	measurement matrix
G, K	geometry matrix and color matrix
K^+	pseudoinverse matrix of K
$\mathbf{w}_i$	color intensity vector
$\rho_\sigma(\alpha)$	micro-facet slope angle distribution
$d^2\Phi_i$, $d^2\Phi_r$	incoming and reflected flux
L_i	radiance
$d\omega_i$, $d\omega'$, $d\omega_r$	various solid angles
dA_s	area of illuminated surface
$F(\theta, \eta, \lambda)$	Fresnel coefficient
$G(\theta_i, \theta_r, \phi_r)$	geometric attenuation factor
$dL_{S,r}$	surface radiance of specular reflection
E_p	image irradiance
d, f	diameter and focal length of a lens

REFERENCES

1. R. Baribeau, M. Rioux, and G. Godin, Color reflectance modeling using a polychromatic laser sensor, *IEEE Trans. Pattern Anal. Machine Intell.* **14**(2), 2, 1992, 263–269.
2. P. J. Besl and N. D. McKay, A method of registration of 3-D shapes, *IEEE Trans. Pattern Anal. Machine Intell.* **14**(2), 1992, 239–256.
3. R. L. Cook and K. E. Torrance, A reflectance model for computer graphics, *ACM Trans. Graphics* **1**(1), 1982, 7–24.
4. H. Delingette, M. Hebert, and K. Ikeuchi, Object modeling by registration of multiple range images, *Image Vision Comput.* **10**(3), 1992.
5. G. Healey, Using color for geometry-insensitive segmentation, *J. Opt. Soc. Am. A* **6**(6), 1989, 920–937.
6. K. Higuchi, M. Hebert, and K. Ikeuchi, Merging multiple views using a spherical representation, in *Proceedings of IEEE CAD-Based Vision Workshop, Champion, 1944*, pp. 123–131.
7. H. Hoppe, T. DeRose, T. Duchamp, J. McDonald, and W. Stuetzle, Surface reconstruction from unorganized points, (SIGGRAPH '92), *Comput. Graphics* **26**(2), 1992, 71–78.
8. B. K. P. Horn and R. W. Sjoberg, Calculating the reflectance map, *Appl. Opt.* **18**(11), 1979, 1770–1779.
9. K. Ikeuchi and K. Sato, Determining reflectance properties of an object using range and brightness images, *IEEE Trans. Pattern Anal. Machine Intell.* **13**(11), 1991, 1139–1153.
10. G. Kay and T. Caelli, Inverting an illumination model from range and intensity maps, *CVGIP: Image Understanding* **59,** 1994, 183–201.
11. H. Lee, E. J. Breneman, and C. P. Schulte, Modeling light reflection for computer color vision, *IEEE Trans. Pattern Anal. Machine Intell.* **12**(4), 1990, 402–409.
12. J. Lu and J. Little, Reflectance function estimation and shape recovery from image sequence of a rotating object, *Proceedings of IEEE International Conference on Computer Vision June 1995*, pp. 80–86.
13. S. K. Nayar, K. Ikeuchi, and T. Kanade, Surface reflection: Physical and geometrical perspectives, *IEEE Trans. Pattern Anal. Machine Intell.* **13**(7), 1991, 611–634.
14. F. E. Nicodemus, J. C. Richmond, J. J. Hsia, I. W. Ginsberg, and T. Limperis, *Geometrical Considerations and Nomenclature for Reflectance*, NBS Monograph 160, Nat. Bureau Standards, Washington DC, Oct. 1977.
15. B. Phong, Illumination for computer-generated pictures, *Comm. ACM* **18**(6), 1975, 311–317.
16. W. H. Press, B. P. Flannery, S. A. Teukolsky, and W. T. Vetterling, *Numerical Recipes in C*, Cambridge Univ. Press, New York, 1988.
17. K. Sato, H. Yamamoto, and S. Inokuchi, Range imaging system utilizing nematic liquid crystal mask, in *Proceedings, International Conference on Computer Vision, 1987*, pp. 657–661.
18. Y. Sato and K. Ikeuchi, Temporal-color space analysis of reflection, *J. Opt. Soc. Am. A* **11**(11), 1994, 2990–3002.
19. Y. Sato and K. Ikeuchi, Reflectance analysis under solar illumination, *Proceedings of IEEE Physics-Based Modeling and Computer Vision Workshop, 1995*, pp. 180–187.
20. S. Shafer, Using color to separate reflection components, *COLOR Res. Appl.* **10**(4), 1985, 210–218.
21. T. M. Strat, Recovering the camera parameters from a transformation matrix, in *Proceedings, DARPA Image Understanding Workshop, 1984*, pp. 264–271.
22. K. E. Torrance and E. M. Sparrow, Theory for off-specular reflection from roughened surfaces, *J. Opt. Soc. Am.* **57,** 1967, 1105–1114.
23. G. Turk and M. Levoy, Zippered polygon meshes from range images, (SIGGRAPH '94), *Comput. Graphics* 1994, 311–318.
24. G. J. Ward, Measuring and modeling anisotropic reflection, (SIGGRAPH '92), *Comput. Graphics* **26**(2), 1992, 265–272.